A Practical Method for Fault Localization in Distribution Feeders Using Smart Meter Waveforms

Younes Seyedi, Lakshan Piyasinghe, and Al Fargnoli
Hubbell Inc.
77 W Port Plaza Dr
St. Louis, MO 63146
Email: yseyedi@hubbell.com

***Abstract*—Knowledge of a fault location on distribution feeders can help the utilities to quickly restore power, minimize outage duration, and even prevent further outages. This paper introduces a practical method for autonomous identification of faulty line segments on medium-voltage (MV) radial feeders. In the proposed approach, smart meters on the low-voltage (LV) side of the feeder transfer a short window of voltage waveform to a cloud platform which analyzes the voltage transients. The Mahalanobis distance is used to derive the boundaries of the fault transients and to determine the stationary sag interval. The faulty segment is identified by detecting significant changes in a derived feature associated with the line segments during the stationary sag interval. The proposed method does not require deployment of MV sensors, and does not rely on the knowledge of the loads and feeder impedance. As a performance metric, false localization rate (FLR) is evaluated for different fault locations in a 35-bus benchmark system. Extensive Monte Carlo simulations using Python and PSCAD show that the resulting FLRs are very low which corroborate effectiveness of the proposed method.**

I. Introduction

Line faults in medium-voltage (MV) distribution feeders are major events that adversely affect the reliability, safety, and efficiency of the power delivery [1]. Accurate fault localization is therefore essential for the utilities to minimize outage duration, reduce operational costs, and carry out preventive protection to avoid further outages. These advantages help the utilities improve their system reliability indices such as System Average Interruption Duration Index (SAIDI) and System Average Interruption Frequency Index (SAIFI) [2].

Different techniques for fault detection and localization in distribution systems have been investigated in recent papers [3]–[12]. In [3], a magnetic field-based fault localization method is tested for locating faults on a 11-kV distribution feeder. However, their method requires deploying magnetic field sensors on the distribution poles and the substation. Laboratory tests for cable fault localization based on traveling waves theory are demonstrated in [4]. Implementation of such methods in real-life networks is expensive and faces many challenges when the feeder is long with many branches and overhead lines.

A fault localization technique is proposed in [5] which assumes that the meters measure voltage and current phasors, and requires that the junction nodes have synchronized measurement capabilities. Having such measurements at all buses is highly costly and in many cases not feasible. The authors in [6] introduce a probabilistic method in which the distribution system is divided into multiple sub-regions and each sub-region detects faults based on the support vector data description. A major challenge of this approach is the impracticality of obtaining representative and labeled fault data across diverse sub-regions.

Moreover, AI-based approaches have been devised to overcome some fault localization challenges in distribution systems [7]–[9]. However, the major limitation in adopting such methods is the need for reliable and high-fidelity training datasets for machine learning algorithms. In practice, such training datasets are hard to obtain. In addition, using the simulated data for training may lead to over-fitting problems and thus the resulting fault localization models may not generalize well to new networks.

Phasor measurement units (PMUs) which transfer high-rate voltage and current synchrophasors have led to phasor-based fault localization methods [10]–[12]. Practically, implementation of such methods is limited mainly due to the problem of PMU placement. Moreover, many feeders have the lack of proper communication infrastructure for streaming high-rate synchrophasor data, and thus, the utilities would undergo a huge communications cost with these methods.

Unlike previous methods, this paper introduces a topology-based localization approach which only requires a short window of synchronized voltage waveform data from smart meters. Hence, it does not require deployment of any extra sensors on the MV side of the feeders. The proposed approach is basically event-triggered in the sense that it does not require streaming of phasors or waveforms. Fig. 1 shows the functional block diagram for the proposed approach. The meters transfer a short window of waveform data to the cloud whenever they detect an anomaly in their input voltages. The developed algorithms analyze waveform datasets before and after fault inception to localize the faulty line segment. This eliminates the need for knowledge of the feeder impedance, and improves the localization accuracy under variable load and distributed energy resources (DERs). The transient analysis and phasor extraction are carried out in the cloud and there is no interference with the traditional protection system. These practical advantages help the utilities to effectively leverage the proposed localization procedure with minimal cost and effort.

979-8-3315-8138-1

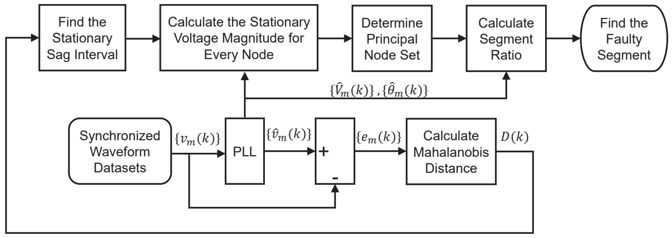

Fig. 1: Step-by-step procedure for fault localization using synchronized voltage waveforms. A bank of PLLs in the cloud platform provides instantaneous error data along with instantaneous voltage magnitude and phase angle at high rate

II. Stationary Voltage Sag Interval

In the case of multi-cycle faults, the meters on the LV side of service transformers observe a sequence of three distinct intervals: 1) A very high perturbation interval upon fault inception. 2) A stationary sag interval that starts shortly after the fault inception. 3) A restoration/collapse interval which starts upon protective actions (tripping) when the voltage gets back to the normal range or zero. The stationary sag interval is a short period of time in which the voltage waveforms have much lower distortions and show a behavior similar to a steady-state condition. Hence, in the stationary sag interval, the voltage magnitude for the fundamental component (i.e., 60 Hz) can be estimated with higher accuracy. To this aim, the boundaries of the stationary sag interval should be determined, which are tied to the abrupt changes in the waveforms. The lower boundary is a function of the fault inception angle and other circuit parameters. The upper boundary, however, depends on the time settings of the operating relay/recloser or the fuses on the laterals. Since such timings are not known beforehand, the cloud platform needs to estimate those boundaries by processing the synchronized waveform datasets.

Suppose that there is a service transformer on each end of the line segments on a radial feeder. Moreover, assume that at least one load is connected to each service transformer which has a smart meter with anomaly detection and synchronized waveform measurement capabilities. The meters transfer a window of N_s waveform samples to the cloud platform upon detection of voltage anomaly. The set of discrete time indices for the waveform collection window is given by:

$$\mathscr{K}_w = \{1, 2, ..., N_s\} \tag{1}$$

and this window spans at least 3 cycles of samples before and after the fault inception. Let $v_m(k)$ denote the k^{th} synchronized voltage sample reported by meter m, where $1 \leq m \leq M$, and M denotes the total number of meters. The instantaneous error data $e_m(k)$ is defined as the difference between the waveform samples $v_m(k)$ and the instantaneous (predicted) fundamental component:

$$e_m(k) = v_m(k) - \hat{v}_m(k), \qquad k \in \mathscr{K}_w \tag{2}$$

The error data for each node is calculated using a bank of phase locked loops (PLLs) [13] as shown in Fig. 1. The PLL bank also extracts the instantaneous voltage magnitude $\hat{V}_m(k)$ and phase angle $\hat{\theta}_m(k)$ based on the input waveform dataset which are used in the localization process as discussed in Section III.

The mean and standard deviation of the error data for the m^{th} meter are estimated as

$$\mu_m = \frac{1}{N_s} \sum_{k \in \mathscr{K}_w} e_m(k) \tag{3}$$

$$\sigma_m = \sqrt{\frac{1}{N_s - 1} \sum_{k \in \mathscr{K}_w} \big(e_m(k) - \mu_m\big)^2} \tag{4}$$

In a real-world scenario, the voltage samples from different meters are spatially correlated, and error vectors can be modeled as multi-variate Gaussian process, i.e., $\mathbf{e} \sim N(\mu, \mathbf{\Sigma})$, where μ is the M-dimensional mean vector, and $\mathbf{\Sigma}$ is the $M \times M$ covariance matrix. The Mahalanobis distance which is a measure of the distance between a sample error vector $\mathbf{e}(k)$ and the underlying multi-variate distribution is calculated as:

$$D(k) = \sqrt{\big(\mathbf{e}(k) - \mu\big)' \mathbf{\Sigma}^{-1} \big(\mathbf{e}(k) - \mu\big)} \tag{5}$$

The abrupt changes in the voltage waveforms of all nodes lead to peaks in the time series of the Mahalanobis distance. In this mechanism, the impact of measurement noise is very low since all the meters are considered at the same time in the processing of the M-distance. The Mahalanobis distance also takes into account the correlations between error data at different nodes, which leads to very good noise robustness in fault inception analysis. Algorithm 1 is used to analyze the time series of the Mahalanobis distance with the aim of finding the stationary sag interval. It should be noted that the primary peak in the time series (corresponding to the fault inception) may not be the global peak. In this algorithm, the parameter k_c shows the number of samples per one cycle of the voltage, e.g., $k_c = \lceil F/60 \rceil$ with F denoting the sampling rate of the voltage waveforms. According to Algorithm 1, the stationary sag interval spans exactly 2 cycles of the voltage waveform after a major part of harmonic distortions is mitigated. Fig. 2 illustrates a faulty voltage waveform from a single meter, and the time series of Mahalanobis distance with primary and secondary peaks identified.

III. Fault Localization

A. Principal Node Set

Once the stationary sag interval has been identified, the stationary voltage magnitude is calculated as the average value of the instantaneous voltage magnitudes over the sag interval:

$$\tilde{V}_m = \frac{1}{|\mathscr{K}_{sag}|} \sum_{k \in \mathscr{K}_{sag}} \hat{V}_m(k) \tag{6}$$

where $\hat{V}_m(k)$ shows the estimated voltage magnitude for node m as estimated by the PLLs (refer to Fig. 1). The averaging in (6) reduces the impact of fluctuations in magnitude estimations due to measurement noise and residual harmonics.

979-8-3315-8138-1

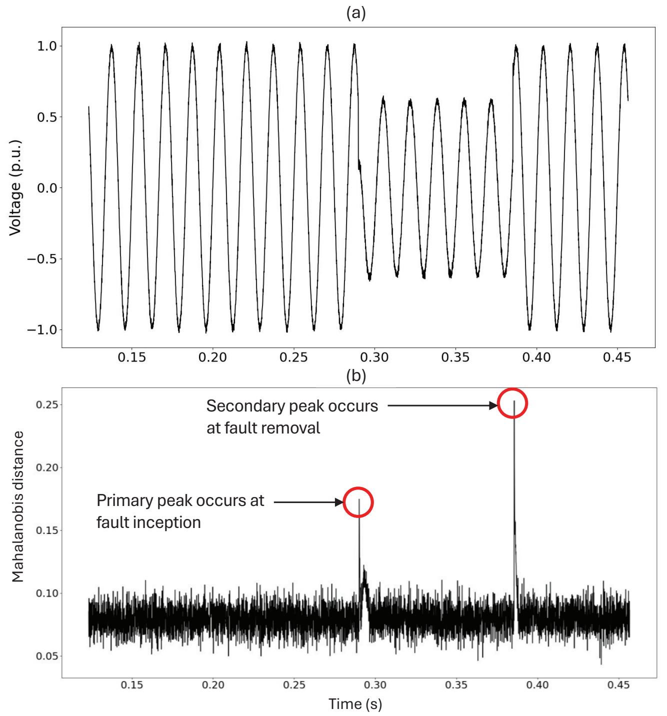

Fig. 2: Identification of abrupt changes in voltage (a): The snapshot of voltage waveform from a single node (b): The estimated Mahalanobis distance

---

Algorithm 1 Stationary Sag Interval

Require: $\mathscr{K}_w$, k_c, $D(k)$

1: Find the first global peak in time series of $D(k)$ and let $k_{gp,1}$ be the sample index of that peak: $k_{gp,1} = \arg\max_{k\in\mathscr{K}_w} D(k)$
2: Define the set of indices as $\mathscr{K}_c = \{k_{gp,1} - k_c, ..., k_{gp,1}, ..., k_{gp,1} + k_c\}$
3: Let $\mathscr{K}_s = \mathscr{K}_w - \mathscr{K}_c$
4: Find the peak in the sub set of $D(k)$ as: $k_{gp,2} = \arg\max_{k\in\mathscr{K}_s} D(k)$
5: Find the primary peak index as: $k_{pp} = \min\{k_{gp,1}, k_{gp,2}\}$
6: Set the stationary sag interval as $\mathscr{K}_{sag} = \{k_{pp} + k_c, ..., k_{pp} + 3k_c\}$ and terminate.

The principal node set is defined as the set containing the minimum voltage node and all of its upstream parent nodes:

$$\mathscr{N} = \left\{o, U\{o\}\right\} \tag{7}$$

$$o = \arg\min_{1\le m\le M} \tilde{V}_m \tag{8}$$

and $U\{o\}$ shows the set of upstream nodes that connect node o to the slack bus on the shortest path. For instance, in the circuit of Fig. 3, the principal node set is $\mathscr{N} = \{1, ..., r-1, r, r+1, ..., o\}$.

B. Segment Ratio Analysis

In radial networks, each pair of adjacent nodes in the principal node set are connected via a feeder segment. The objective of the segment ratio analysis is to distinguish the faulty segment from the healthy segments that encompass the principal node set. First, the normal interval is defined

$$\mathscr{K}_{norm} = \{k_{pp} - 2k_c - 1, ..., k_{pp} - 1\} \tag{9}$$

where the index k_{pp} is determined in step 5 of Algorithm 1. According to (9), the normal interval contains the time indices for the last 2 cycles of waveform data immediately before the fault inception and note that $|\mathscr{K}_{norm}| = |\mathscr{K}_{sag}|$.

Consider a line segment between two adjacent nodes p and q that belong to the principal node set. The segment ratio for this line segment, denoted by $\rho_{p,q}$, is defined as the ratio of average current magnitude in the sag interval over the average current magnitude in the normal interval. Mathematically,

$$\rho_{p,q} = \frac{\sum_{k\in\mathscr{K}_{sag}} \left|\hat{V}_p(k)e^{j\hat{\theta}_p(k)} - \hat{V}_q(k)e^{j\hat{\theta}_q(k)}\right|}{\sum_{k\in\mathscr{K}_{norm}} \left|\hat{V}_p(k)e^{j\hat{\theta}_p(k)} - \hat{V}_q(k)e^{j\hat{\theta}_q(k)}\right|} \tag{10}$$

As discussed in the Appendix, the variations of $\rho_{p,q}$ are tied to the location of end nodes p and q relative to the fault location. Hence, to find the faulty segment, we calculate the segment ratio for all segments from the principal node set and evaluate changes starting from the end node o and moving backward to the slack bus. The faulty segment is the first segment which shows a large jump to a positive number in segment ratio compared to the immediate downstream segment. Algorithm 2 shows the implementation of the segment ratio analysis to find the faulty segment. In this algorithm, parameter Γ represents the threshold for jumps in the segment ratio for the adjacent nodes in $\mathscr{N}$.

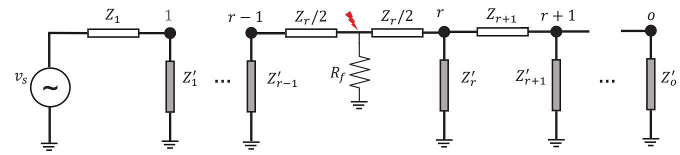

Fig. 3: The circuit diagram of a feeder that has a fault in the middle of the line segment $\overline{r-1, r}$. Z'_m and Z_m respectively show the service impedance and the feeder impedance in p.u. Node o has the minimum stationary voltage magnitude

IV. Simulation Results

A. Benchmark System

A simulation benchmark system was designed based on a real distribution feeder in the United States and implemented in PSCAD [14]. The benchmark system is a 7.2 kV radial feeder with 35 service transformers and spot loads ($M = 35$), and a shunt capacitor bank as shown in Fig. 4. The feeder segments (s_i) have typical ASCR conductors with the ampacity of 200 A. The segments have different lengths ranging from 0.02 mile up to 0.45 mile as given in Table I. The fault simulation framework consists of Python packages and the PSCAD automation library. The Python package generates the fault parameters, creates the load profile, runs PSCAD time-domain simulations, and executes the localization algorithm

979-8-3315-8138-1

Algorithm 2 Finding the Faulty Segment

Require: $\mathscr{N}$, Γ

For every pair of neighboring nodes p and q from $\mathscr{N}$ calculate the segment ratio $\rho_{p,q}$ using (10)
if $\rho_{|\mathscr{N}-1|,|\mathscr{N}|} > \Gamma$ **then**, set the faulty line as $\overline{|\mathscr{N}-1|, |\mathscr{N}|}$ and terminate.
else
  Set $p = |\mathscr{N}-2|$ and go to 5
  While $p > 1$:
  if $\rho > \Gamma$ and $\rho < \Gamma$ **then**, set the faulty line as $\overline{p+1, p+2}$ and terminate.
  else
    Set $p \leftarrow p - 1$
  end if
end if

based on the simulated waveforms. In each time-domain run, a random line-to-ground fault with duration of at least 3 cycles and low impedance is simulated using the benchmark system. White Gaussian noise is added to the simulated waveforms based on a signal-to-noise ratio (SNR) of 80 dB, which is typical for modern smart meters. Unless otherwise stated, the threshold for the segment ratio analysis is $\Gamma = 3$.

B. Discussion of the Numerical Results

Extensive Monte Carlo simulations have been carried out to assess the performance of the proposed localization method. Table I shows the false localization rate (FLR) when the line faults occur at different segments of the test feeder. For each fault location, 10000 datasets of noisy voltage waveforms are simulated under variable load demand to ensure that the localization accuracy is assessed under realistic conditions.

For 28 line segments, the FLR is smaller than 0.01 which indicates the proposed method is accurate for more than 99% of times when faults occur on those lines. For the line segments $s_4 - s_7$, and $s_9, s_{13}, s_{15}, s_{21}$ the FLR is relatively larger and is higher than 0.01. It should be noted that this lower localization accuracy is due to the electrical characteristics of those segments of the feeder. In fact, those 8 lines are very short and possess smaller impedance, hence the measurement noise has a larger impact on the segment ratio for them. However, for those shorter lines, if the the localization algorithm pinpoints

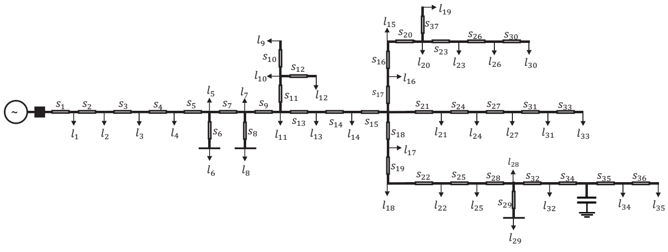

Fig. 4: The single-line diagram of the simulation benchmark system developed in PSCAD

TABLE I: The FLRs for random faults at different locations

Line Segment	Length (miles)	FLR	Line Segment	Length (miles)	FLR
s_2	0.09	0.0014	s_{20}	0.25	0.0001
s_3	0.07	0.0028	s_{21}	0.32	0.0448
s_4	0.05	0.0969	s_{22}	0.26	0.0005
s_5	0.06	0.0196	s_{23}	0.4	0
s_6	0.03	0.9758	s_{24}	0.32	0.0001
s_7	0.02	0.9692	s_{25}	0.45	0.0003
s_8	0.75	0	s_{26}	0.34	0
s_9	0.03	0.7774	s_{27}	0.32	0
s_{10}	0.2	0	s_{28}	0.26	0.0003
s_{11}	0.2	0.0001	s_{29}	0.28	0
s_{12}	0.08	0.0011	s_{30}	0.4	0
s_{13}	0.05	0.1334	s_{31}	0.32	0
s_{14}	0.15	0.0006	s_{32}	0.26	0.0003
s_{15}	0.04	0.8196	s_{33}	0.32	0
s_{16}	0.1	0.0002	s_{34}	0.26	0
s_{17}	0.13	0.0002	s_{35}	0.29	0.0001
s_{18}	0.05	0.0006	s_{36}	0.22	0
s_{19}	0.08	0.001	s_{37}	0.27	0

TABLE II: The average distance to the fault location

Line Segment	Average Distance (mile)
s_4	0.06
s_5	0.055
s_6	0.045
s_7	0.04
s_9	0.057
s_{13}	0.04
s_{15}	0.098
s_{21}	0.18

to another segment, for most of the times the result is an adjacent segment and the identified location is not very far from the actual fault location. Table II shows the average distance to the fault location when the fault occurs on those shorter lines. The average distance is derived by calculating the average of the distance between the actual fault location and the middle point of the detected segment when the detected segment differs from the faulty segment. It is seen that in the case of false localization, only a small area around the detected segment would need to be investigated for faults.

V. Conclusion

This paper presents a practical method for online identification of faulty line segments in MV radial feeders. The proposed approach employs synchronized voltage waveforms from smart meters on the LV side of feeders, and analyzes them in a cloud-based platform. Faulty segments are detected through variations in the phasor-based features of the lines within the extracted stationary sag interval. Simulation results on a 35-bus benchmark system demonstrate low false localization rates, validating the method's effectiveness and accuracy.

Appendix

This appendix explains the basic premise behind Algorithm 2 for finding the faulty section. First, we define the parameter

979-8-3315-8138-1

α_m as:

$$\alpha_m = \frac{\sum_{k \in \mathscr{K}_{sag}} \hat{V}_m(k)}{\sum_{k \in \mathscr{K}_{norm}} \hat{V}_m(k)}, \qquad m \in \mathscr{N} \tag{11}$$

Without loss of generality, assume that the fault occurs in the middle of segment $\overline{r-1,r}$, as depicted in Fig. 3. If the node p is downstream node r and q is downstream node p, then the following relationship holds in the phasor domain for both stationary sag and normal intervals:

$$\hat{V}_q(k)e^{j\hat{\theta}_q(k)} = \frac{Z_{eq,q}}{Z_{eq,q}+Z_q}\hat{V}_p(k)e^{j\hat{\theta}_p(k)} \tag{12}$$

Noting that p and q are two adjacent nodes from $\mathscr{N}$, and $Z_{eq,q}$ shows the equivalent impedance for the feeder part which is downstream the node q. From (12) and (10), the segment ratio is written as:

$$\rho_{p,q} = \alpha_p, \quad p,q \in \mathscr{N}_D \tag{13}$$

where $\mathscr{N}_D$ shows the subset of the principal node set that contains nodes downstream the node r. On the other hand, the voltage magnitude maintains the following inequality:

$$\hat{V}_p(k|k \in \mathscr{K}_{sag}) < \hat{V}_p(k|k \in \mathscr{K}_{norm}) \tag{14}$$

Using (14) in Eq. (11), and since $|\mathscr{K}_{norm}| = |\mathscr{K}_{sag}|$, the following relationship holds:

$$\rho_{p,q} < 1, \quad p,q \in \mathscr{N}_D \tag{15}$$

Now consider the segment between the nodes $r-1$ and r which incurs the fault as depicted in Fig. 3. The following equation is valid for the stationary sag interval:

$$\hat{V}_r(k)e^{j\hat{\theta}_r(k)} = \frac{Z_{eq,r}R_f\hat{V}_{r-1}(k)e^{j\hat{\theta}_{r-1}(k)}}{\frac{Z_r}{2}(R_f+\frac{Z_r}{2}+Z_{eq,r})+R_f(\frac{Z_r}{2}+Z_{eq,r})}, \; k \in \mathscr{K}_{sag} \tag{16}$$

where $Z_{eq,r}$ is the equivalent impedance for the feeder part which is downstream the node r. It is noted that during the normal (pre-fault) interval, there is no shunt resistance R_f, and the following equation holds:

$$\hat{V}_r(k)e^{j\hat{\theta}_r(k)} = \frac{Z_{eq,r}\hat{V}_{r-1}(k)e^{j\hat{\theta}_{r-1}(k)}}{Z_r+Z_{eq,r}}, \; k \in \mathscr{K}_{norm} \tag{17}$$

Based on Eqs. (10), (16) and (17), and after some mathematical manipulations, the segment ratio for the faulty segment is derived as follows:

$$\rho_{r-1,r} = \beta_r \times \alpha_{r-1} \tag{18}$$

$$\beta_r = \frac{\left|\frac{Z_r}{Z_r+\frac{R_f Z_{eq,r}}{R_f+\frac{Z_r}{4}+\frac{Z_{eq,r}}{2}}}\right|}{\left|\frac{Z_r}{Z_r+Z_{eq,r}}\right|} \tag{19}$$

For low-impedance faults where $R_f \to 0^+$, we have

$$\left|\frac{Z_r}{Z_r+\frac{R_f Z_{eq,r}}{R_f+\frac{Z_r}{4}+\frac{Z_{eq,r}}{2}}}\right| \to 1^- \tag{20}$$

Moreover, the feeder impedance is much smaller than the equivalent impedance for node r, i.e., $|Z_r| << |Z_{eq,r}|$. Therefore, we can conclude that:

$$\left|\frac{Z_r}{Z_r+Z_{eq,r}}\right| \to 0^+ \tag{21}$$

Based on (20) and (21) it is seen that the coefficient β_r given in (19) is significantly larger than unity. Whereas the value of α_{r-1} is smaller than unity. Therefore, the values of the segment ratio for every segment downstream the fault are:

$$\begin{aligned} \rho_{o-1,o} &= \alpha_{o-1}, \\ \rho_{o-2,o-1} &= \alpha_{o-2} \\ &\vdots \\ \rho_{r,r+1} &= \alpha_r \\ \rho_{r-1,r} &= \beta_r \times \alpha_{r-1} \end{aligned} \tag{22}$$

In practice, due to noise and harmonics, the values of α_m may fluctuate and slightly go beyond unity, however, the coefficient β_r in $\rho_{r-1,r}$ leads to a large jump in the segment ratio.

REFERENCES

[1] J. Wang, et al., "Smart Fault Detection, Classification, and Localization in Distribution Networks: AI-Driven Approaches and Emerging Technologies", *IEEE Access*, vol. 13, pp. 141664 – 141693, Aug. 2025

[2] IEEE Standard 1366-2022, "IEEE Guide for Electric Power Distribution Reliability Indices," IEEE Power and Energy Society, Nov. 2022.

[3] M. Kazim, et al., "Fault Detection and Localization for Overhead 11-kV Distribution Lines With Magnetic Measurements", *IEEE Trans. Instrumentation and Measurement*, vol. 69, no. 5, pp. 2028 – 2038, May 2020

[4] F. Zavoda, et al., "Fault localization system for medium voltage distribution underground network" *in Proc. of* 27th International Conference on Electricity Distribution, Jun. 2023.

[5] A. Bharti, et al., "Fault Localization Technique in Smart Active Distribution System with Data Uncertainties", *in Proc. of* 4th International Conference on Power, Control and Computing Technologies, Jan. 2025

[6] Z. Lin, et al., "Data-Driven Fault Localization in Distribution Systems with Distributed Energy Resources", *in Proc. of* IEEE Sustainable Power and Energy Conference, Nov. 2019

[7] M. Zhao, and M. Barati, "A Real-Time Fault Localization in Power Distribution Grid for Wildfire Detection Through Deep Convolutional Neural Networks", *IEEE Trans. Industry Applications*, vol. 57, no. 4, pp. 4316-4326, July-Aug. 2021

[8] J. Shang, et al., "An Enhanced Fault Localization Method in Distribution Network Using Graph Neural Network", *in Proc. of* 20th International Conference on Natural Computation, Fuzzy Systems and Knowledge Discovery, Jul. 2024

[9] A. Tamrakar, and S. Sarangi, "Intelligent Algorithms for Fault Localization in Unbalanced Active Distribution System" *in Proc. of* IEEE International Conference on Power Electronics, Drives and Energy Systems, Dec. 2024

[10] F. Conte, et al., "Fault Detection and Localization in Active Distribution Networks Using Optimally Placed Phasor Measurements Units", *IEEE Trans. Power Systems*, vol. 38, no. 1, pp. 714 – 727, Jan. 2023

[11] D. Liang, et al., "Efficient Two-Stage Fault Localization for Distribution Networks with Optimally Placed μPMUs", *IEEE Trans. on Smart Grid*, Early Access, 2025

[12] D. Sodin, et al., "Precise PMU-Based Localization and Classification of Short-Circuit Faults in Power Distribution Systems", IEEE Trans. Power Delivery, *IEEE Trans. Power Delivery*, vol. 38, no. 5, pp. 3262 – 3273, Oct. 2023

[13] H. Karimi, Y. Seyedi, and M. Karimi-Ghartemani, "A Robust and Simple Phase-Locked Loop for Unbalanced Power Grid Applications" *in Proc. of* IEEE 28th International Symposium on Industrial Electronics (ISIE), Jun. 2019

[14] Manitoba HVDC Research Centre, PSCAD/EMTDC, Winnipeg, MB, Canada. Available Online: https://www.pscad.com

979-8-3315-8138-1